

# A high-resolution rotation curve of NGC 6822: a test-case for cold dark matter

D. T. F. Weldrake,<sup>1</sup> W. J. G. de Blok<sup>2★†</sup> and F. Walter<sup>3‡</sup>

<sup>1</sup>Research School of Astronomy & Astrophysics, Mount Stromlo Observatory, Cotter Road, Weston Creek, ACT 2611, Australia

<sup>2</sup>Australia Telescope National Facility, PO Box 76, Epping NSW 1710, Australia

<sup>3</sup>California Institute of Technology, Astronomy Department 105-24, Pasadena, CA 91125, USA

Accepted 2002 October 9. Received 2002 August 28; in original form 2002 July 25

## ABSTRACT

We present high-resolution rotation curves of the Local Group dwarf irregular galaxy NGC 6822 obtained with the Australia Telescope Compact Array. Our best curves have an angular resolution of 8 arcsec or 20 pc and contain some 250 independent points. The stellar and gas components of NGC 6822 cannot explain the shape of the curve, except for the very inner regions, and NGC 6822 is consequently very dark-matter-dominated. There is no evidence for the presence of a steep density cusp down to scales of  $\sim 20$  pc, contrary to the predictions of cold dark matter.

**Key words:** galaxies: dwarf – galaxies: fundamental parameters – galaxies: individual: NGC 6822 – galaxies: kinematics and dynamics – Local Group – dark matter.

## 1 INTRODUCTION

NGC 6822 is a dwarf irregular Local Group member. Located at a distance of  $490 \pm 40$  kpc (Mateo 1998), NGC 6822 is the most nearby dwarf irregular apart from the Large/Small Magellanic Cloud (LMC/SMC) system. Owing to the small distance the galaxy appears very extended on the sky: its optical angular diameter is over a quarter of a degree; the H I disc measures close to a degree (de Blok & Walter 2000). NGC 6822 is a member of an extended cloud of irregulars (Mateo 1998) known as the ‘Local Group Cloud’. The galaxy has a total luminosity of  $M_B = -15.8$  (Hodge et al. 1991) and a total H I mass of  $1.3 \times 10^8 M_\odot$  (de Blok & Walter 2000), making it relatively gas-rich. It is a metal-poor galaxy, with an interstellar medium (ISM) abundance of approximately  $0.2 Z_\odot$  (Skillman, Terlevich & Melnick 1989) and has a star formation rate of  $\sim 0.06 M_\odot \text{ yr}^{-1}$  [based on H $\alpha$  and far-infrared (FIR) fluxes] (Mateo 1998; Israel, Bontekoe & Kester 1996). Hodge (1980) found evidence for increased star formation between 75 and 100 Myr ago, while Gallart et al. (1996) showed that the star formation in NGC 6822 increased by a factor of 2–6 between 100 and 200 Myr ago. This is consistent with the mostly constant but stochastic recent star formation histories often derived for dwarf and low surface brightness (LSB) galaxies (Grebel 2001; Gerritsen & de Blok 1999). NGC 6822 can be regarded as a rather average and quiescent dwarf irregular galaxy.

de Blok & Walter (2001) found that the outer H I disc is dominated by what appears to be a supergiant H I shell with extended,

apparently tidal features in the outer disc. In contrast, the inner main H I disc is remarkably uniform and circularly symmetric. There is no evidence for large kinematical disturbances, as we will show in this paper.

In this paper we address the detailed dynamics and kinematics of NGC 6822 and derive high-resolution rotation curves of this dwarf galaxy. The physical resolution of our highest-resolution curve is  $\sim 20$  pc or  $\sim 0.03h$ , where  $h$  is the exponential scalelength of the stellar disc (see Section 6.1), making it the highest-resolution H I rotation curve of any undisturbed dwarf galaxy.

In Section 2 we summarize the ‘small-scale crisis’ in current cosmological simulations. Section 3 briefly describes the observations and data reduction, while Sections 4 and 5 describe the derivation and analysis of the rotation curves in detail. In Section 6 we describe the models used in rotation curve fitting, while Section 7 presents the results. Section 8 discusses the results, and tries to fit them in the cold dark matter (CDM) picture. We summarize our conclusions in Section 9.

## 2 DARK MATTER IN DWARFS

Cosmological numerical cold dark matter simulations predict a specific and universal shape for the dark matter mass–density distributions (and therefore the rotation curves) of galaxies (Dubinski & Carlberg 1991). This was investigated in detail by Navarro, Frenk & White (1996, 1997) who found that the mass–density distribution in the inner parts of simulated CDM haloes could be best described by an  $r^{-1}$  power law. This steeply increasing density cusp towards the centre naturally translates into a steeply rising rotation curve. This kind of curve is, however, not observed in late-type disc galaxies (e.g. Swaters 1999; Verheijen 1997). The rotation curves of dwarf and

\*E-mail: Erwin.deBlok@astro.cf.ac.uk

†Present address: Department of Physics and Astronomy, Cardiff University, Queen’s Buildings, PO Box 913, Cardiff CF24 3YB.

‡Present address: NRAO AOC, PO Box O, 1003 Lopezville Road, Socorro, NM 87801-0387, USA.

LSB galaxies are shallow and rise linearly, more consistent with a dark matter distribution that is dominated by a constant-density core with a size of a few kpc (Moore 1994; de Blok & McGaugh 1997; de Blok et al. 2001b; Blais-Ouellette, Amram & Carignan 2001). In particular in the case of LSB galaxies there has been much discussion concerning the reality of the observed shallow curves (Swaters, Madore & Trewheella 2000). It was argued that systematic resolution effects ('beam-smearing') could hide the steep CDM curves and lead to an erroneous conclusion that they would not be consistent with CDM.

Subsequent high-resolution follow-up studies, measuring the rotation curves of LSB galaxies in H $\alpha$  at a resolution of  $\sim 0.2$  to  $\sim 1$  kpc have now confirmed the conclusions derived from the early data (de Blok et al. 2001b; de Blok, McGaugh & Rubin 2001a; McGaugh, Rubin & de Blok 2001; Bosma & de Blok 2002; Blais-Ouellette et al. 2001; Bolatto et al. 2002). Dwarfs and LSB galaxies seem to be dominated by a dark matter distribution that is best described in the inner parts by a power law  $\rho \sim r^\alpha$  with  $\alpha = -0.2 \pm 0.2$  (de Blok et al. 2001b).

With a spatial resolution of only  $\sim 20$  pc, the current data set enables us to measure the rotation curve of this dwarf galaxy at a resolution that is an order of magnitude better than the observations described above. Among other things, the high resolution makes it possible to investigate the effect beam size has on mass models and test whether the inferred distribution of dark matter depends on resolution.

### 3 OBSERVATIONS AND DATA REDUCTION

NGC 6822 was observed with the Australia Telescope Compact Array for  $15 \times 12$  h in its 375 ( $1 \times 12$  h), 750D ( $2 \times 12$  h), 1.5A ( $4 \times 12$  h), 6A and 6D ( $8 \times 12$  h) configurations over the period from 1999 June to 2000 March. A total of eight pointings was observed covering the entire H I extent of the galaxy. We used a bandwidth of 4 MHz with a channel separation of  $0.8 \text{ km s}^{-1}$ . Additionally, to obtain zero-spacing information, NGC 6822 was observed with the Parkes single-dish radio telescope using the multibeam receiver in its narrow-band mode in 1998 December. The correlator configuration was identical to that used for the Compact Array observations.

The data were reduced and mosaicked together using the MIRIAD data reduction package. Super-uniform weighting, reducing side lobes in individual pointings prior to mosaicking, was used. The resulting data cubes were cleaned with the MIRIAD MOSSDI task. We combined the single-dish and synthesis data to correct for the missing zero-spacings and produced data cubes at various spatial and velocity resolutions. For the rotation curve analysis presented here we use the data cubes with channel separations of  $1.6 \text{ km s}^{-1}$  (with an effective velocity resolution of  $1.9 \text{ km s}^{-1}$ ). These cubes gave the best compromise between velocity resolution and signal-to-noise ratio.

We analysed the  $1.6 \text{ km s}^{-1}$  data at five different spatial resolutions. The synthesized beam sizes used were  $96 \times 349.4$ ,  $48 \times$

$174.7$ ,  $24 \times 86.4$ ,  $12 \times 42.4$  and  $8 \times 28.3 \text{ arcsec}^2$ . The position angle of the beam was  $0^\circ$  at all resolutions. We will refer to the five different resolution data sets as B96, B48, B24, B12 and B08, respectively. Table 1 gives some more information on the data sets. We retained the elliptical beam shape to obtain the highest possible resolution along the major axis. As the PA of the major axis of NGC 6822 is  $\sim 110^\circ$ , as shown later, this means that the resolution along the major axis is to a few per cent equal to the minor axis beam size. The large size of the galaxy compared with the beam rules out any beam-smearing effects caused by non-major axis information entering the beam.

### 4 MOMENT MAPS AND VELOCITY FIELD

All subsequent analysis was done using the GIPSY package. The low-resolution cube B96 was clipped at the  $2\sigma$  level, and remaining noise peaks were removed by hand. Then for B48 and subsequent resolutions, we used the  $2\sigma$ -clipped cube of the previous resolution as a mask, after which remaining spurious noise peaks were removed by hand. This ensures a consistent selection of features at all resolutions. Furthermore, using the lower-resolution cube as a mask ensures that possible extended low-level structures are retained in the map.

The integrated H I surface density maps were made in the usual manner by adding together all clipped channel maps. As a second step we then isolated the high signal-to-noise (S/N) ratio regions of the maps as follows. For uniformly tapered maps in velocity  $\sigma_{\text{tot}} = \sqrt{N}\sigma_{\text{ch}}$ , where  $\sigma_{\text{tot}}$  is the noise in a pixel in the integrated column density map,  $N$  is the number of channels contributing to that pixel and  $\sigma_{\text{ch}}$  is the noise in one channel at that pixel. We constructed noise maps for each integrated column density map, and used these together with the column density maps to isolate those pixels in the column density maps where  $S/N > 10$ . These high signal-to-noise ratio maps were used as masks for the velocity fields. Fig. 1 shows the integrated column density map derived for the B12 data.

There are two standard ways to produce a velocity field. One commonly used procedure is to determine the intensity-weighted mean of the velocities along each profile. It is known that this method can produce spurious velocities at low resolution and low S/N ratios. Given the high resolution and S/N ratio of our data set, this is unlikely to be a problem here. An alternative method is to fit (a) Gaussian(s) to each profile. The latter method usually gives better results, as it is less affected by systematic effects owing to skewed profiles, etc. It is, however, computationally more expensive, which becomes important for data cubes of the size we are dealing with here. The high quality of the current data puts us firmly in the regime where the intensity-weighted mean gives accurate results.

To test this we have compared both methods for the B12 data set (Fig. 2) and find that for our data the differences are negligible. A histogram of the differences is very well described by a Gaussian with an average of  $-0.3 \text{ km s}^{-1}$  and an rms of  $1.0 \text{ km s}^{-1}$ , i.e. both methods produce identical results to within better than a channel

**Table 1.** Data cube properties.

	B96	B48	B24	B12	B08
Beam size (arcsec)	$349.4 \times 96$	$174.7 \times 48$	$86.4 \times 24$	$42.4 \times 12$	$28.3 \times 8$
Pixel size (arcsec)	$32 \times 32$	$16 \times 16$	$8 \times 8$	$4 \times 4$	$2.5 \times 2.5$

Note: all data cubes presented here have a channel separation of  $1.6 \text{ km s}^{-1}$ , and an effective velocity resolution of  $1.9 \text{ km s}^{-1}$ .

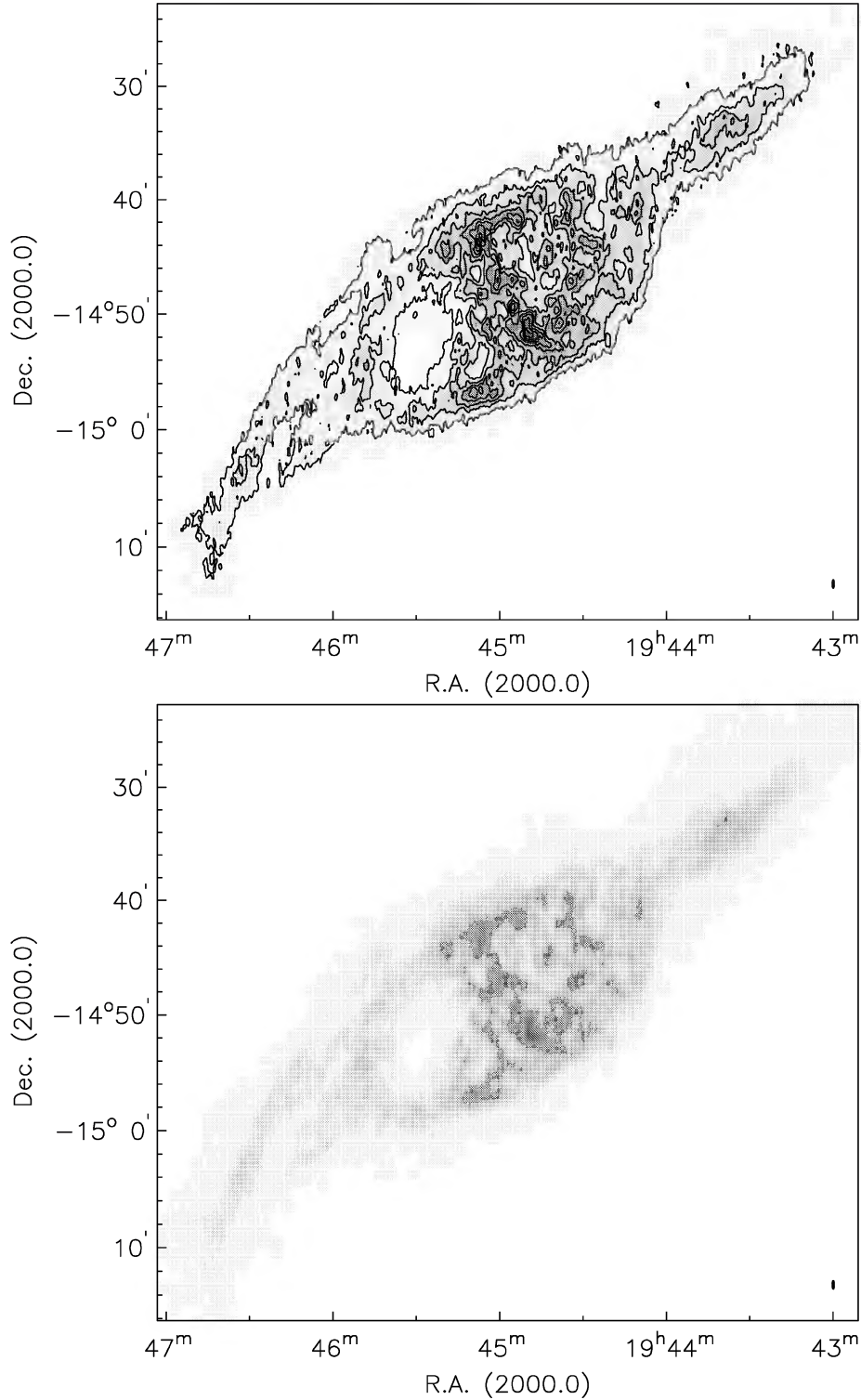
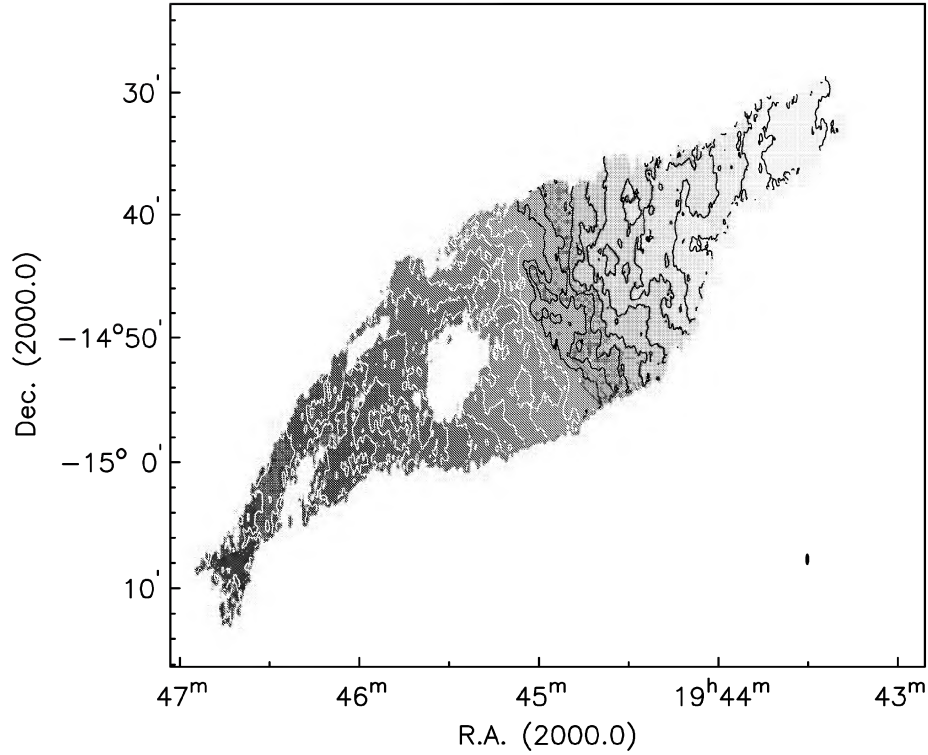


**Figure 1.** B12 total column density map. Contours start at  $5 \text{ M}_{\odot} \text{ pc}^{-2}$  and increase in steps of  $1 \text{ M}_{\odot} \text{ pc}^{-2}$ . The beam is indicated in the lower right-hand corner.

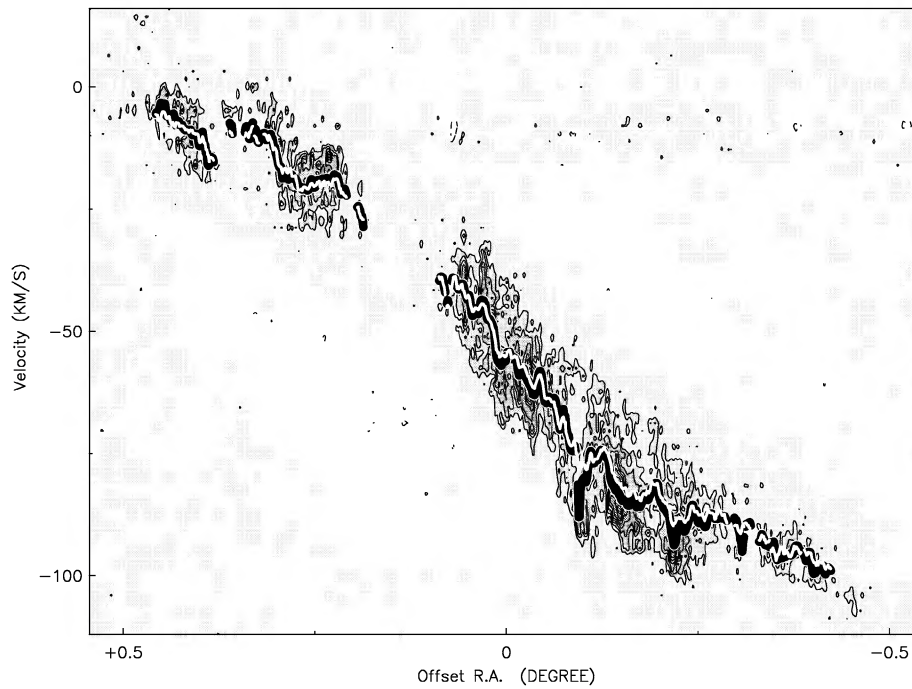
spacing. The number of pixels where the residuals reach  $5 \text{ km s}^{-1}$  or higher is only  $\sim 0.1$  per cent of the total number of pixels.

Fig. 3 shows a major axis position velocity diagram of the B12 data, taken along a position angle of  $120^{\circ}$ . Overplotted are the veloci-

ties as found in the intensity-weighted and Gaussian velocity fields. The velocity fields produce the same results, without large-scale systematic deviations. We will therefore proceed to use intensity-weighted velocity fields in subsequent analysis.



**Figure 2.** The intensity-weighted velocity field, derived from the B12 data. The black contours run from  $-55 \text{ km s}^{-1}$  in the central parts to  $-100 \text{ km s}^{-1}$  in the outer NW parts, in steps of  $5 \text{ km s}^{-1}$ . The white contours run from  $-50 \text{ km s}^{-1}$  in the inner parts to  $+10 \text{ km s}^{-1}$  in the outer SE parts. The beam is shown in the lower right-hand corner.



**Figure 3.** B12 data major axis position–velocity diagram taken along position angle  $120^\circ$ . Dotted contour represents  $-4\sigma$ , full contours start at  $4\sigma$  and increase in steps of  $2\sigma$ . The white line shows the values found in the intensity-weighted velocity field. The black line shows values derived from the Gaussian velocity field.



## 5 DERIVING ROTATION CURVES

The rotation curves were produced using the GIPSY task ROTCUR. For a well-resolved and high S/N ratio data set such as the current one, the tilted ring procedure is by far the best way to determine the rotation curve. Other methods that are often used, such as adjusting the tilted ring parameters by hand using position velocity diagrams as a guide (e.g. using the GIPSY command INSPECTOR), are more subjective and results can depend on guesses on, for example, the magnitude and effects of beam smearing.

From Fig. 2 we can see that the high-resolution velocity fields contain an extraordinary amount of detail. To obtain a good feel for the large-scale structure in NGC 6822 we started by deriving the B96 rotation curve, and used the results for each resolution as the initial estimate for the next higher resolution, thus gradually refining the curve.

We adopted rings with a width equal to the minor axis of the beam. The beam is elongated roughly along the minor axis of NGC 6822 with an effective radius of  $\sim 1.9$  times the minor axis. A ring width equal to the minor axis is a good compromise between beam shape and complete sampling. Most information contributing to the rotation curve comes from near the major axis where the beam is narrow.

In general, the procedure involved making a fit with all parameters [systemic velocity, centre position, position angle (PA), inclination and rotation velocity] free. The central position and systemic velocity were then fixed and several runs with either inclination or PA or both fixed were made to find the best model.

As the minor axis generally provides little information regarding the rotation curve we excluded an angle of  $30^\circ$  around the minor axis from the fits. One usually also down-weights the data around the minor axis by applying a  $|\cos \theta|$  weighting, where  $\theta$  is the angle with respect to the major axis in the plane of the galaxy. Other alternatives are to apply a uniform weighting or a  $\cos^2 \theta$  weighting. We have experimented with different weighting schemes and varying the exclusion angle around the minor axis between  $15^\circ$  and  $45^\circ$ , but found no difference in the curves produced (this is caused by the large number of independent points that *do* contribute at full weight around the major axis). We therefore adopt a uniform weighting scheme and a free angle around the minor axis of  $30^\circ$ .

Once a satisfactory curve using both sides of the velocity field was produced, we also calculated two curves using only the approaching and receding sides of the velocity field. Comparing the three curves gives information concerning the symmetry of the system.

### 5.1 The rotation curves

For each resolution we derived the curve using the procedure described above. The results are shown in Table 2 and Fig. 4. The trends

found in PA and inclination for the different resolutions agree well with each other. Only the B96 data does not show the PA trend as strongly. The variation of inclination with radius is only small; only the highest resolutions show weak evidence of a slight warp in the outer parts: choosing a constant inclination instead therefore does only marginally affect the curves. The trend in PA is pronounced and real; deriving curves with a constant PA results in velocities and inclinations that are inconsistent with the data, especially at the higher resolutions. The small-scale kinks in the inclination are not physical and are mainly caused by dispersion effects.

Beyond  $R \sim 1000$  arcsec (2.5 kpc) the difference between the approaching and receding sides becomes more pronounced with increasing resolution. This radius corresponds to the edge of the inner H I disc. The receding curve shows no significant features there, but the approaching curve shows a dip in velocity. This coincides with the interface between the main H I disc and the NW cloud (de Blok & Walter 2001). However, at larger radii the receding curve converges with the approaching one, indicating that the galaxy and cloud (NW side) and the ‘tails’ (SE side) are embedded in one symmetrical halo. The global dynamics of the system appear undisturbed despite the morphology of the H I. The small kink at  $R \sim 150$  arcsec (0.38 kpc) is caused by a number of high-velocity dispersion regions that over a small radial range happen to be aligned with the tilted rings. At  $R \sim 500$  arcsec a similar small kink corresponds with the inner edge of the large hole.

Fig. 5 shows an overlay of the rotation curve on various position–velocity slices. The rotation curve is a good representation of the dynamics of the galaxy as a whole.

For all resolutions we have compared the velocity fields with model velocity fields constructed from the tilted ring fits, and find no systematic large-scale residuals. Fig. 6 compares the B12 velocity fields. There are only a few localized regions of slightly higher residuals in the higher-resolution models, coinciding with regions of high velocity dispersion. Other resolutions give similar results.

### 5.2 Final curves

The error bars derived from the tilted ring fits are an indication of the scatter in velocity around the best-fitting velocity at each tilted ring. As such they do not take into account large-scale asymmetries, differences between approaching and receding sides, etc. To define more realistic errors, we regard the absolute difference between the rotation velocities of the approaching and receding sides as  $2\sigma$  errors. We adopt the maximum of the tilted ring uncertainties and the asymmetry uncertainties as our error bars, with one further modification. In some cases both sides of the galaxy are very symmetrical, and these usually are also the radii where the tilted ring uncertainties are very small. These combine to give very small errors ( $\ll 0.1$  km s $^{-1}$ ). We have therefore imposed a minimum error of half a channel

**Table 2.** Adopted ROTCUR parameters.

	B96	B48	B24	B12	B08
XPOS	19 <sup>h</sup> 44 <sup>m</sup> 57 <sup>s</sup> .54	19 <sup>h</sup> 44 <sup>m</sup> 58 <sup>s</sup> .76	19 <sup>h</sup> 44 <sup>m</sup> 58 <sup>s</sup> .71	19 <sup>h</sup> 44 <sup>m</sup> 58 <sup>s</sup> .04	19 <sup>h</sup> 44 <sup>m</sup> 58 <sup>s</sup> .91
YPOS	−14°49′13″.0	−14°49′17″.6	−14°49′21″.7	−14°49′18″.9	−14°49′23″.8
VSYS	−53.3 km s $^{-1}$	−54.7 km s $^{-1}$	−54.7 km s $^{-1}$	−54.4 km s $^{-1}$	−54.6 km s $^{-1}$
PA	0–1248: 109° 1344–2592: 109°–138°	0–480: 127°–105° 480–2400: 105°–130°	0–480: 130°–105° 480–2136: 105°–131°	0–456: 140°–103° 456–1992: 103°–130°	0–480: 150°–106° 480–680: 106° 688–1992: 106°–130°
INCL	58°:7	59°:9	58°:7	0–1056: 58° 1056–1992: 58°–68°	0–1096: 57° 1104–1992: 57°–68°

Notes. Italics indicate a range in radius in arcsec. The pair of numbers following it indicate the linear range in parameter over this radial range.

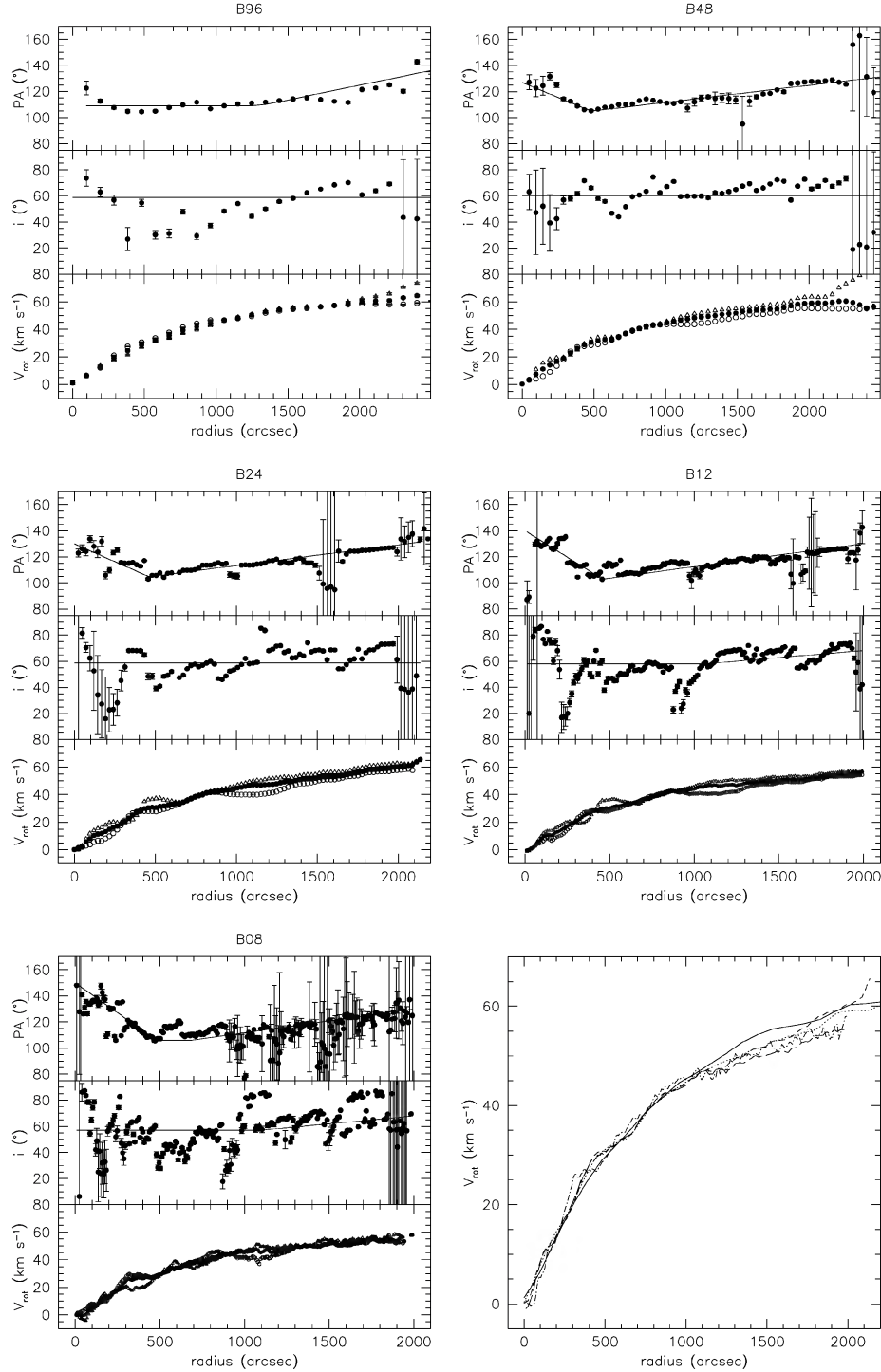


**Figure 4.** Results of the tilted ring fits for the B96, B48 (top row), B24, B12 (middle row) and B08 (bottom-left) resolutions. In each panel we show the position angle of the major axis (top), the inclination (centre) and circular velocity (bottom) as a function of radius for the various resolutions. In every bottom subpanel the filled circles represent the curve derived using the whole velocity field. The open circles represent the curve for the approaching (SE) side, while the triangles represent the receding (NW) side. Overplotted in the top and centre subpanels are the models used to derive these curves. The points in the top subpanel show the behaviour of PA as a free parameter, with inclination fixed to its model value as shown in the centre panel. The points in the centre subpanel show the behaviour of inclination with PA fixed to the model values as shown in the top panel. The bottom-right panel shows the rotation curves at each resolution overplotted. Full line: B96; dotted line: B48; short-dashed line: B24; long-dashed line: B12; dash-dotted line: B08.

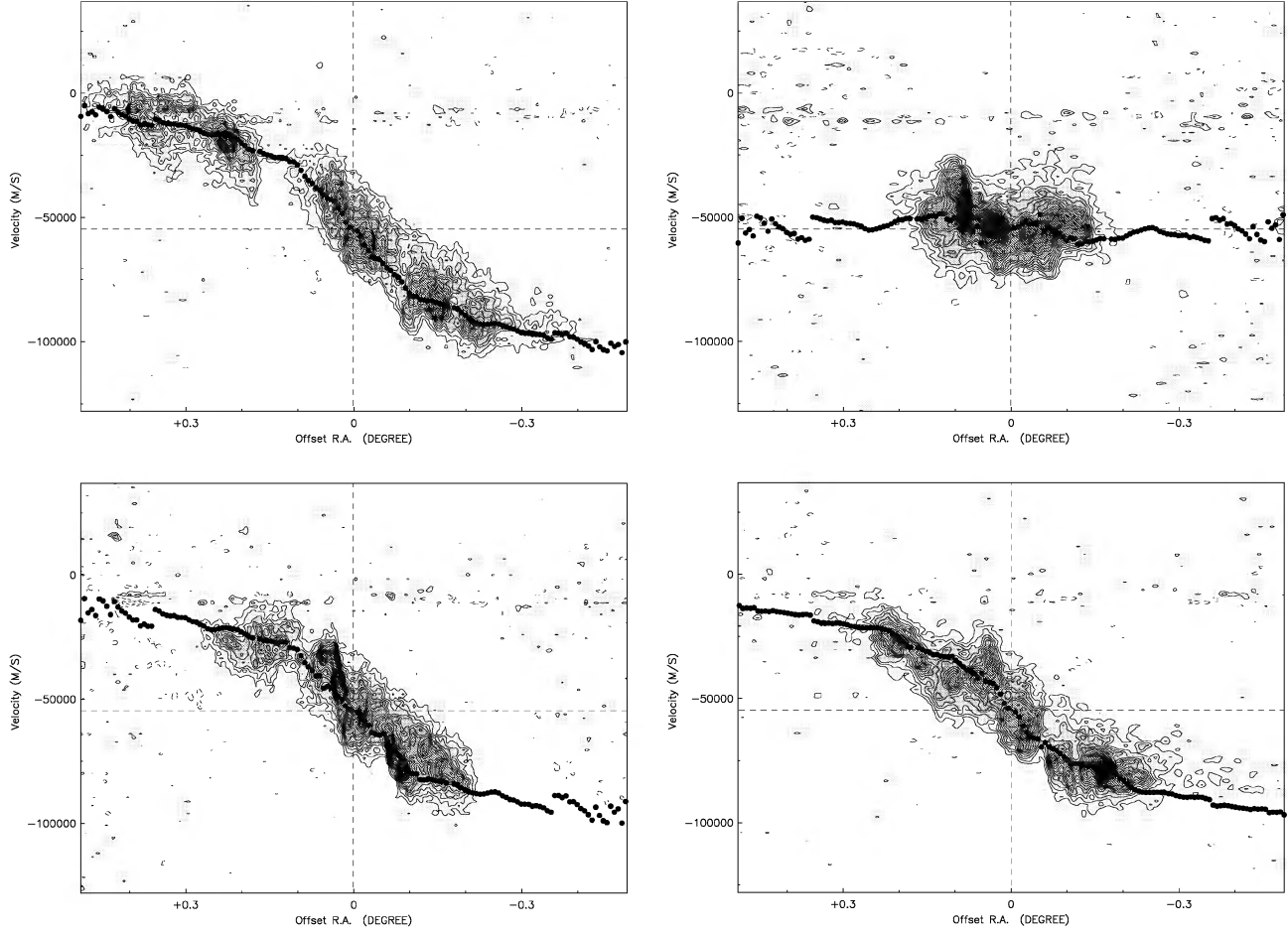


**Figure 5.** Position velocity slices of the B24 data, with the projected rotation curve overplotted. The full contours are plotted starting at  $3\sigma$  in steps of  $2\sigma$ . The dotted contours show the  $-3\sigma$  and  $-5\sigma$  levels. There is residual Milky Way emission present at  $\sim -10 \text{ km s}^{-1}$ . The dotted lines represent the centre of the galaxy and the systemic velocity. Overplotted is the final curve as derived from the tilted ring fits, corrected to the position angle of the slice. Top left: major axis position-velocity slice taken at a position angle of  $115^\circ$ . Top right: minor axis position-velocity slice. Bottom left: position angle of major axis minus  $30^\circ$ . Bottom right: position angle of major axis plus  $30^\circ$ . NGC 6822 is, despite the disturbed morphology, a very symmetrical galaxy.

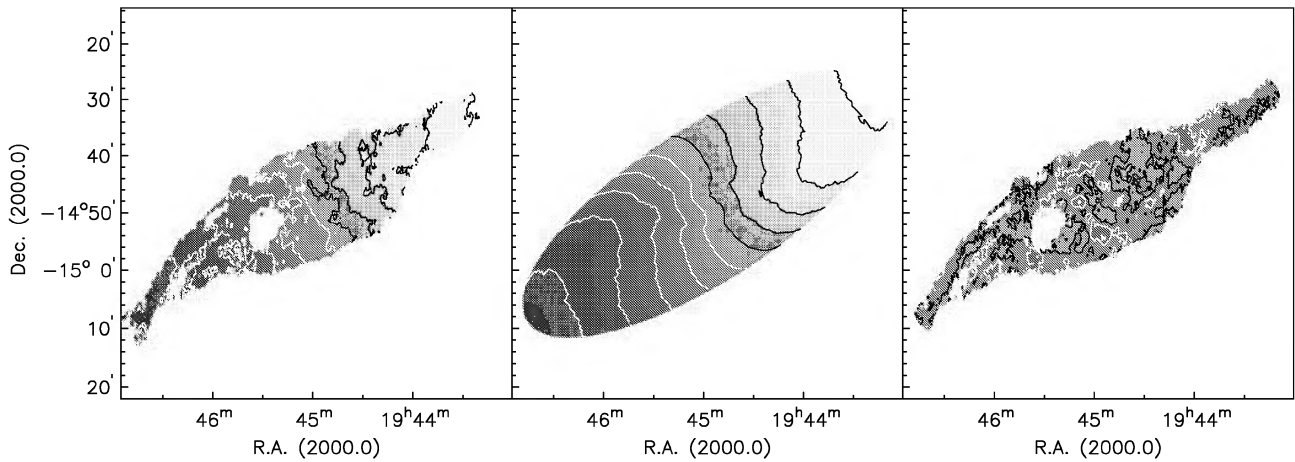


**Figure 6.** Comparison of the observed velocity fields (left-hand column) and the circularly symmetric model velocity fields derived from the tilted ring fits (centre column). The white velocity contours start in the centre of the velocity field at  $-50 \text{ km s}^{-1}$  and increase in steps of  $10 \text{ km s}^{-1}$ . The black contours start in the centre at  $-55 \text{ km s}^{-1}$  and decrease in steps of  $10 \text{ km s}^{-1}$  towards the NW. The right most column shows the residual velocity field (observed-tilted ring). The first white contour represents  $+5 \text{ km s}^{-1}$  and subsequent white contours increase with a step of  $5 \text{ km s}^{-1}$ . The first black contour shows the  $-5 \text{ km s}^{-1}$  and subsequent black contours decrease in steps of  $5 \text{ km s}^{-1}$ .

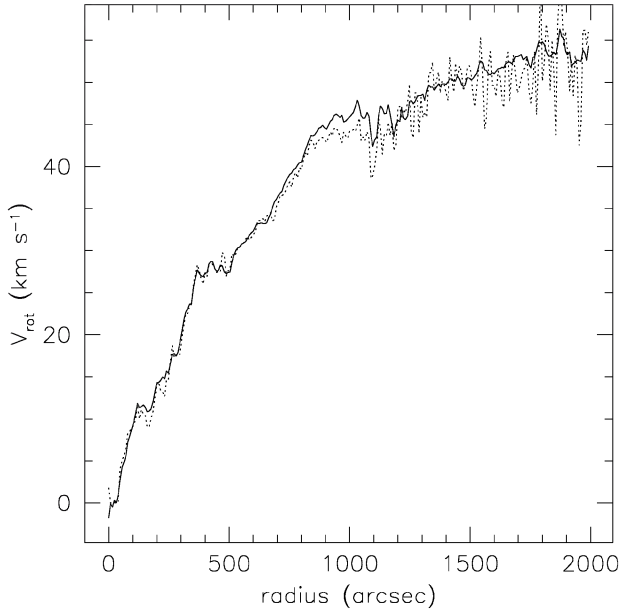


**Figure 7.** The B08 rotation curve (solid line) and corrected for asymmetric drift (dotted line).

width on the curves. After corrections for inclination this translates to a minimum error of  $0.8 \text{ km s}^{-1}$ .

In principle, the H I rotation curves also need to be corrected for the pressure gradients in the gas to derive the true rotation velocities. This correction for asymmetric drift is given by

$$v_c^2 = v_\phi^2 - \sigma^2 \left( \frac{\partial \ln \rho}{\partial \ln R} + \frac{\partial \ln \sigma^2}{\partial \ln R} \right),$$

where  $v_c$  is the true rotation velocity,  $v_\phi$  is the observed gas rotation velocity,  $\sigma$  is the velocity dispersion in the gas and  $\rho$  is the volume density. The median (modal) velocity dispersion in the disc of NGC 6822 is  $\sim 5.8$  ( $\sim 5.7$ )  $\text{km s}^{-1}$ , as measured in the  $1.6 \text{ km s}^{-1}$  channel spacing data, and does not show any obvious radial trends. Assuming a constant scaleheight, we can derive the correction for asymmetric drift. We consider the B08 curves where, owing to the large gradients in the H I surface density, the corrections are largest. The corrected and uncorrected curves are shown in Fig. 7. Both curves are very similar, with the largest corrections of  $\sim 3 \text{ km s}^{-1}$  occurring between 850 and 1050 arcsec. It should be borne in mind that the correction itself is also uncertain and depends on assumptions of, for example, constant scaleheight, which may not hold in the outer parts of the gas disc. As the uncertainties caused by asymmetric drift in the inner parts are negligible, ignoring them will not affect the results. Based on this analysis, we decided not to apply this correction.

### 5.3 Dynamical centres

The central position as derived above varies slightly from resolution to resolution. This is understandable given the different beam sizes. Fig. 8 shows the central positions overplotted on a B12 column density map of NGC 6822, where the error bars span the major- and minor-axis FWHM of the respective beams. Also plotted are K-band 2MASS (see below) and R-band isophotal centres. Owing to the large size, low galactic latitude and the irregular morphology the optical centre in NGC 6822 is difficult to determine. From different fits performed at various isophotal levels we estimate an uncertainty

## High-resolution rotation curve of NGC 6822 19

of  $\sim 0.5$  arcmin. These positions are offset from the dynamical centre by approximately 105 arcsec or 0.25 kpc.

Though the dynamical centre is *by definition* the zero-point of the rotation curve, it is instructive to rederive the rotation curve under the assumption that the optical centre is the true centre of the galaxy. This is implicitly assumed in many emission-line observations of rotation curves where the optical centre of the galaxy is frequently used to line up the slit of the spectrograph. We rederived the B12 rotation curve, fixing the position of the centre to that of the optical centre. We kept the run of position angle and inclination identical to that in the original model. Fig. 9 overplots the two curves. The overall shape of the curve is insensitive to the precise position of the centre. The small-scale differences are of the same order of magnitude as the differences between the approaching and receding sides of the original curve. One should, however, not exaggerate the importance of this offset: had NGC 6822 been at a more typical distance of a few tens of Mpc, then the angular size of the offset would only be  $\sim 1$  arcsec and would have been unnoticed.<sup>1</sup>

## 6 MASS COMPONENTS

### 6.1 Stellar component

We used a mosaic of full-resolution 2MASS  $K_s$  images to derive the surface brightness profile of NGC 6822. The orientation parameters and the centres of the tilted ring fits to the velocity fields were used to measure the average surface brightness at each radius. Prior to the ellipse integration bright stars were masked out. The average surface brightness contribution of remaining foreground stars in the field away from NGC 6822 was determined and subtracted from the profile.

The  $K_s$  surface brightness of NGC 6822 is low and at large radii the scatter is substantial. At radii beyond 750 arcsec the signal of the galaxy can no longer be distinguished from the sky background. Fig. 10 shows the azimuthally averaged surface brightness profile, corrected for inclination, determined using the B08 tilted ring parameters. The surface brightness was corrected for Galactic foreground extinction, though this was only a small correction of 0.088 mag in the  $K$  band. We assumed NGC 6822 to be optically thin in  $K$ , and only applied a geometric inclination surface brightness correction.

The profile can be well described by an exponential disc. As the outer parts of the profile could be marginally affected by small uncertainties in the sky background we have fitted an exponential disc to the profile at  $R < 400$  arcsec and find an exponential scalelength of 286 arcsec or 0.68 kpc. The central surface brightness is  $\mu_0(K_s) = 19.8 \text{ mag arcsec}^{-2}$ . We derive the total absolute magnitude assuming an exponential disc and extrapolating to infinity gives  $M_K = -17.9$  or  $L_K = 3.8 \times 10^8 L_\odot$ .

For each resolution we determine the surface brightness profiles using the relevant tilted ring parameters determined. At  $R > 240$  arcsec we replace the surface brightness profiles with that of the exponential disc fit as indicated in Fig. 10. The rotation curve of the stellar disc was then computed from the extended  $K$ -band profile

<sup>1</sup> As an aside, we refer ahead to the discussion on central mass–density slopes in Section 8.1, where we determine the power-law slope  $\alpha$  of the mass–density profile  $\rho \sim r^\alpha$  within a radius of 0.8 kpc. For the B12 case we find a slope of  $\alpha = -0.04 \pm 0.09$ . For the curve presented here, determined using the optical centre and also using an outer radius of 0.8 kpc, a similar analysis gives  $\alpha = -0.23 \pm 0.24$ . The uncertainties are larger, but the value is consistent with a soft core in NGC 6822. The exact position of the dynamical centre does not significantly influence the results.



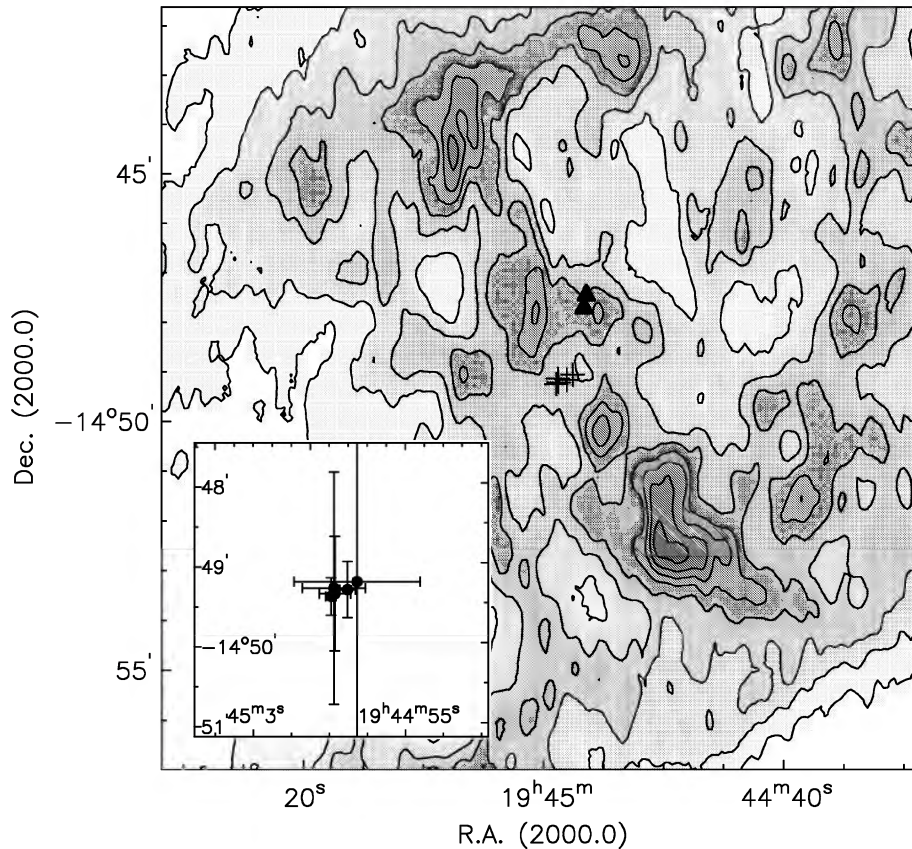


**Figure 8.** Positions of the dynamical centres of the five resolutions (crosses) overplotted on the B12 total column density map. Contours start at  $5 \text{ M}_{\odot} \text{ pc}^{-2}$  and increase in steps of  $1 \text{ M}_{\odot} \text{ pc}^{-2}$ . The triangles show the positions of the  $K$  band isophotes (top) and  $R$  band isophotes (bottom). The inset more clearly shows the relative positions of the dynamical centres. Error bars span the FWHM beam. The centres all coincide to better than a beamwidth.

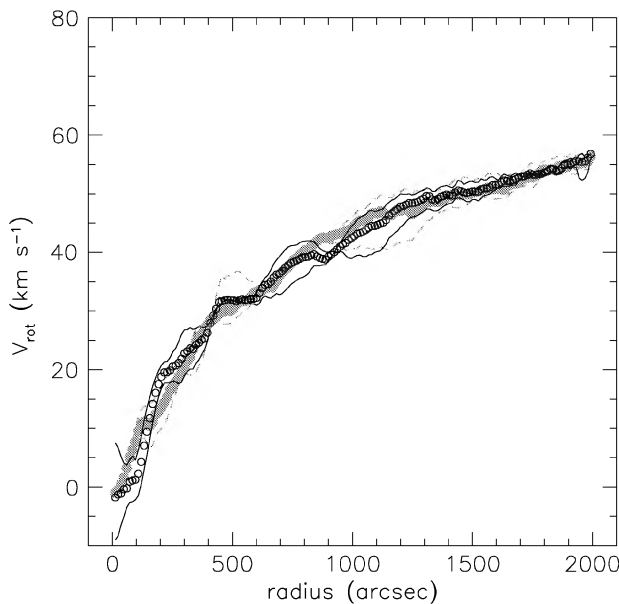


**Figure 9.** Comparison of the B12 rotation curves derived using the true dynamical centre as the central position (grey curves), and using the  $K$ -band optical centre as the central position (black curves). The thin lines represent the curves from the approaching and receding sides separately.

following Casertano (1993) and Begeman (1987). The disc was assumed to have a vertical  $\text{sech}^2$  distribution with a scaleheight  $z_0 = h/6$  (van der Kruit & Searle 1981). The rotation curves of the stellar component were sampled at the same radii as the rotation curves. We assume  $\Upsilon_*$  is constant with radius. While one expects some modest variation in  $\Upsilon_*$  with radius in optical bands (de Jong 1996), the colour gradients in dwarf LSB galaxies in the  $K$  band tend to be small, so this effect is not likely to be significant (see also Section 6.4).

## 6.2 Gas component

We used the orientation parameters of the tilted ring fits to determine the azimuthally average H I surface density profiles using the total column density maps for each resolution. The H I surface density profiles are presented in Fig. 11. In deriving the corresponding rotation curve with the GPSY task ROTMOD we scaled the surface density profiles by a factor of 1.4 to take the contribution of helium and metals into account.

We assume that the gas is distributed in an infinitely thin disc. This assumption is not crucial. Though one might expect dwarf galaxies to have a more puffed up disc than a typical spiral galaxy, the shape and amplitude of the gas rotation curve depends only very mildly on the thickness of the disc.

To use the B12 curve as an example, for the infinitely thin gas disc case the maximum rotation velocity of the gas component is

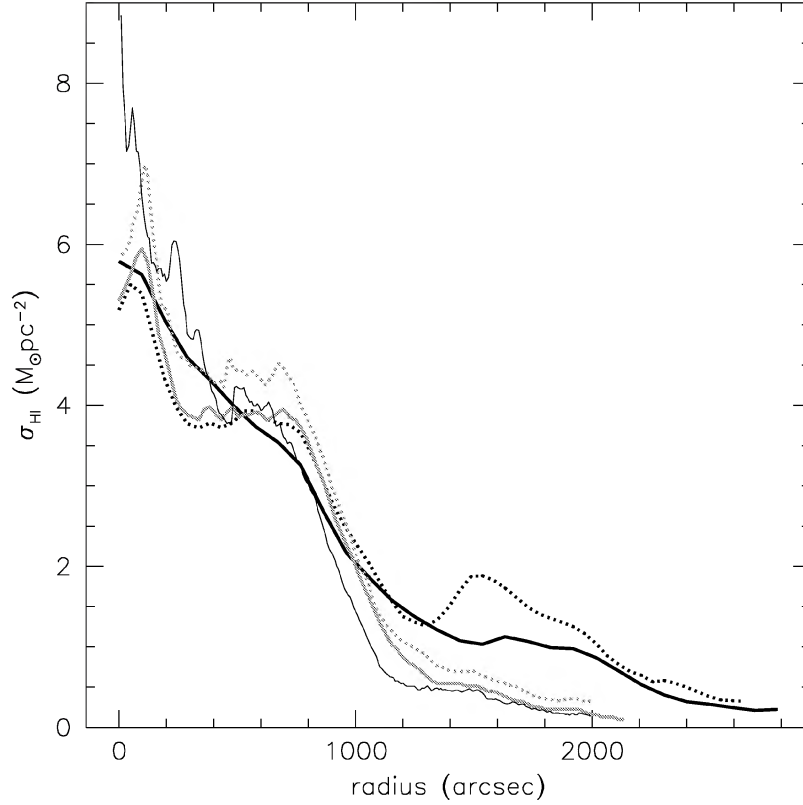


**Figure 10.** Azimuthally averaged  $K$ -band surface brightness profile. The profile is corrected for inclination and Galactic foreground extinction. Spacing between the points is 8 arcsec. The line indicates the exponential disc fit used at radii  $R > 240$  arcsec.

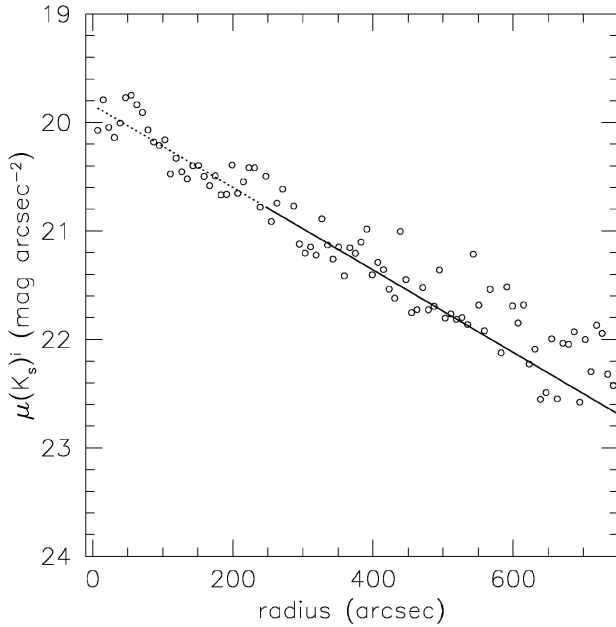


**Figure 11.**  $H\text{I}$  surface density profiles, corrected for inclination. The various resolutions are distinguished as follows: B96, full thick black line; B48, dotted thick black line; B24, full grey thick line; B12, dotted grey thick line; B08, full thin black line.

$17 \text{ km s}^{-1}$ . When increasing the thickness of the disc, this maximum rotation velocity drops only very slowly: for an exponential scaleheight  $z = 0.5 \text{ kpc}$ , it still measures  $\sim 14.5 \text{ km s}^{-1}$ . This value for  $z$  is already approaching the value of the radial scalelength of the stellar distribution and is probably already too large. We thus adopt the thin-disc approximation.

### 6.3 Halo models

The dark halo component differs from the previous two in that we are interested in parametrizing this component assuming some fiducial model. The choice of this model is the crux of most of the DM analyses in the literature, and many models exist. These can all be broadly distinguished into two groups: halo models with a core and halo models with a cusp. An example of the first category is the pseudo-isothermal halo, an example of the latter the CDM NFW halo.

#### 6.3.1 Pseudo-isothermal halo

The spherical pseudo-isothermal (ISO) halo has a density profile

$$\rho_{\text{ISO}}(R) = \frac{\rho_0}{1 + (R/R_C)^2}, \quad (1)$$

where  $\rho_0$  is the central density of the halo and  $R_C$  is the core radius of the halo. The corresponding rotation curve is given by

$$V(R) = \sqrt{4\pi G \rho_0 R_C^2 \left[ 1 - \frac{R_C}{R} \arctan\left(\frac{R}{R_C}\right) \right]}. \quad (2)$$

The asymptotic velocity of the halo,  $V_\infty$ , is given by

$$V_\infty = \sqrt{4\pi G \rho_0 R_C^2}. \quad (3)$$

To characterize this halo only two of the three parameters ( $\rho_0$ ,  $R_C$ ,  $V_\infty$ ) are needed, as equation (3) determines the value of the third parameter.

### 6.3.2 NFW halo

The NFW mass–density distribution takes the form (Navarro et al. 1996)

$$\rho_{\text{NFW}}(R) = \frac{\rho_0}{(R/r_0)[1 + (R/r_0)]^2}, \quad (4)$$

where  $r_0$  is the characteristic radius of the halo and  $\rho_0$  is the characteristic density (Navarro et al. 1996; Blais-Ouellette et al. 2001). This mass distribution gives rise to a halo rotation curve

$$V(R) = V_{200} \left\{ \frac{\ln(1 + cx) - cx/(1 + cx)}{x[\ln(1 + c) - c/(1 + c)]} \right\}^{1/2}, \quad (5)$$

where  $x = R/R_{200}$ . It is characterized by a concentration parameter  $c = R_{200}/R_s$  and a radius  $R_{200}$ . These are directly related to  $R_s$  and  $\rho_i$ , but are used instead as they are a convenient way to parametrize the rotation curve. The radius  $R_{200}$  is the radius where the density contrast exceeds 200 (roughly the virial radius; Navarro et al. 1996). The characteristic velocity  $V_{200}$  of the halo is defined in the same way as  $R_{200}$ . These parameters are not independent and are set by the cosmology.

### 6.4 Stellar mass-to-light ratios and weighting

One of largest uncertainties in any mass model is the value of the stellar mass-to-light ratio  $\Upsilon_*$ . Though broad trends in  $\Upsilon_*$  have been measured and modelled (e.g. Bottema 1997; Bell & de Jong 2000), the precise value for an individual galaxy is not well known, and depends on extinction, star formation history, the initial mass function, etc. The value of  $\Upsilon_*$  cannot be constrained using the rotation curve alone (van Albada & Sancisi 1986; Lake & Feinswog 1989) and some assumptions must be made. We therefore present disc–halo decompositions using four different assumptions.

(i) Minimum disc. This model assumes that the observed rotation curve is due entirely to DM. This gives an upper limit on how concentrated the dark mass component can actually be. It is not a realistic model per se, because it ignores the gas disc that is obviously present. However, we present it here for ease of comparison with cosmological simulations, a large fraction of which tend to only model the dark matter component.

(ii) Minimum disc + gas. The contribution of the atomic gas (H I and He) is taken into account, but  $\Upsilon_*$  is assumed to be zero.

(iii) Constant  $\Upsilon_*$ . Here we choose a value for  $\Upsilon_*$  appropriate for NGC 6822 based on its stellar content, colours and likely star formation history. Unfortunately reliable integrated colours for NGC 6822 are rare owing to its large angular size. We can, however, use indirect arguments to arrive at a value for  $\Upsilon_*$ . Furthermore, we are interested here only in the  $K$ -band value, which is rather insensitive to the effects of extinction and recent star formation.

Verheijen (1997) presents  $K'$ -band rotation curve fits of a large sample of high surface brightness (HSB) and LSB galaxies in the Ursa Major cluster. We consider the rotation curve fits derived using the Bottema disc prescription (Bottema 1997). This recipe states that the maximum rotation velocity of the disc is 63 per cent of the maximum rotation velocity observed (and is derived from measurements of stellar velocity dispersions). The distribution of  $\Upsilon_{*K}$  ratios derived with the Bottema disc for the dwarf and LSB galaxies in the UMa sample peaks at  $\Upsilon_{*K} = 0.4 \pm 0.05$ . If the colours of NGC 6822 are comparable to those found for other dwarfs and LSB galaxies (namely  $B - V \sim 0.5$ ,  $B - R \sim 0.8$  and  $V - I \sim 0.8$ ; de Blok, van der Hulst & Bothun 1995) we can use table 3 in Bell & de Jong (2000) to derive an approximate value for  $\Upsilon_*$ . For their formation epoch model with burst we find values for  $\Upsilon_{*K}$  between 0.35 and 0.40. Similar values are found for the infall models and the hierarchical models. From detailed population synthesis modelling of NGC 6822, Gallart et al. (1996) find that the total mass of stars and stellar remnant ever formed in NGC 6822 must be  $\sim 9 \times 10^7 M_\odot$ . Combined with the  $K$ -band luminosity derived earlier, this gives a value  $\Upsilon_{*K} = 0.24$ .

Taking the above into account we adopt a value of  $\Upsilon_{*K} = 0.35$  as representative of the stellar population in NGC 6822.

(iv) Maximum disc. The rotation curve of the stellar component is scaled to the maximum value allowed by the observed rotation curve, but with the restriction that the DM density gradient is required to be flat or negative at all radii (thus avoiding a ‘hollow halo’) (van Albada & Sancisi 1986).

Each of the rotation curves was fitted using the GIPSY task ROTMAS. The program determines the best-fitting combination of  $R_C$  and  $V_\infty$  (for the pseudo-isothermal halo) or  $c$  and  $V_{200}$  (for the NFW halo), using a least-squares fitting routine. We assigned weights to the data points inversely proportional to the square of their uncertainty.

## 7 RESULTS

Figs 12–16 show the rotation curves at all resolutions plotted for the four assumptions on  $\Upsilon_*$  for both NFW and ISO halo models. To rule out the possibility that the outer parts of NGC 6822, which might be affected by tidal effects, affect our conclusions we also present separate fits to just the inner part of the galaxy out to  $R = 1000$  arcsec (2.4 kpc) or the edge of the main inner disc. Tables 3 and 4 present the fitting parameters for all models presented here.

An inspection of Tables 3 and 4 shows that the goodness of fit is in all cases better for ISO than for NFW. The only exceptions are some of the maximum disc fits where both ISO and NFW are difficult to fit, as NGC 6822 is not a maximum disc galaxy. A comparison between the  $\chi^2$  values is shown in Fig. 17.

The maximum disc values of  $\Upsilon_*$  generally have an uncertainty of  $\pm \sim 0.1$ . Changing the values within this range has no discernible effect on the quality of the fits. One point of note is that for the B08 case the maximum disc value for  $\Upsilon_*$  is less than that for the constant- $\Upsilon_*$  case. The B08 constant  $\Upsilon_*$  fit thus results in a hollow halo.

Many of the NFW fits have fitting parameters that do not make physical sense. The large majority of the fits prefer  $c \leq 0$  and  $V_{200} \rightarrow \infty$ , which is another way of saying that the fitting procedure is trying to fit a  $V \sim R^{1/2}$  curve to a  $V \sim R$  curve by stretching it to infinity, thus trying to take out the curvature in the model. Where this happened we fixed the  $c$  parameter to  $c = 0.1$  with only  $V_{200}$  as the free parameter. Such a value is still outside the range predicted by cosmological simulations where values of  $c \sim 10$  would be expected.

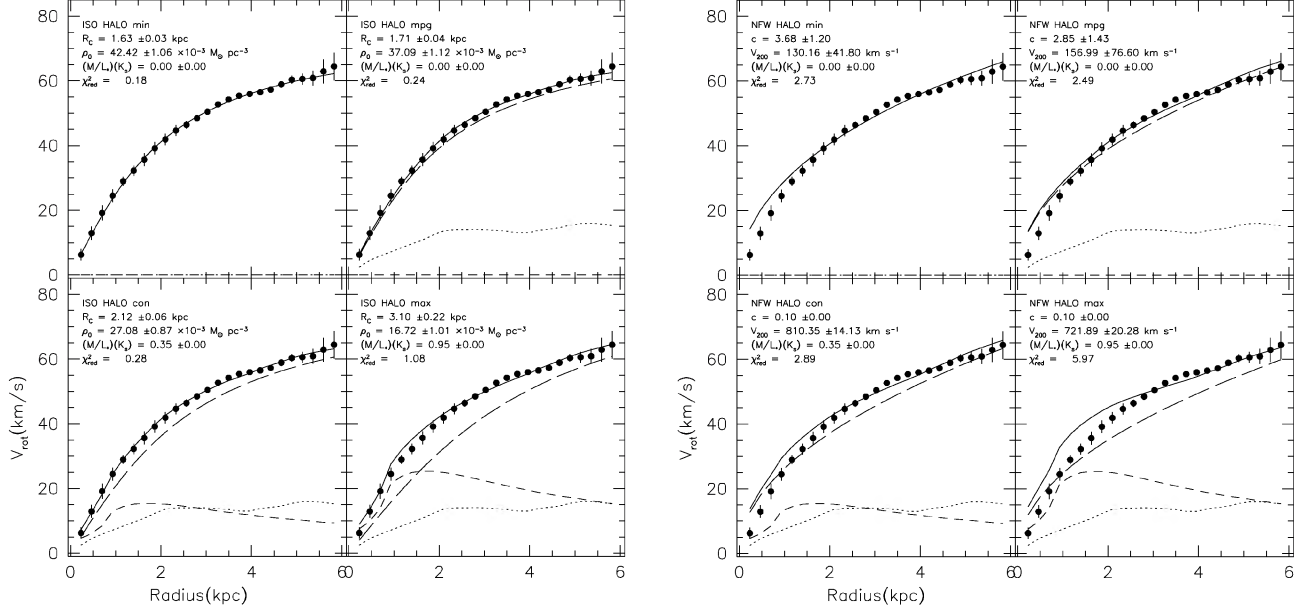


**Figure 12.** B96 mass models. The left-hand column shows the fits made using a pseudo-isothermal halo. The right-hand column shows the NFW halo fits. In each panel the following fits are shown: minimum disc (top left), minimum disc + gas (top right), constant  $\Upsilon_*$  (bottom left) and maximum disc (bottom right). Fitting parameters are given in the subpanels. An error of ‘0.00’ indicates that this parameter was fixed during the fitting.

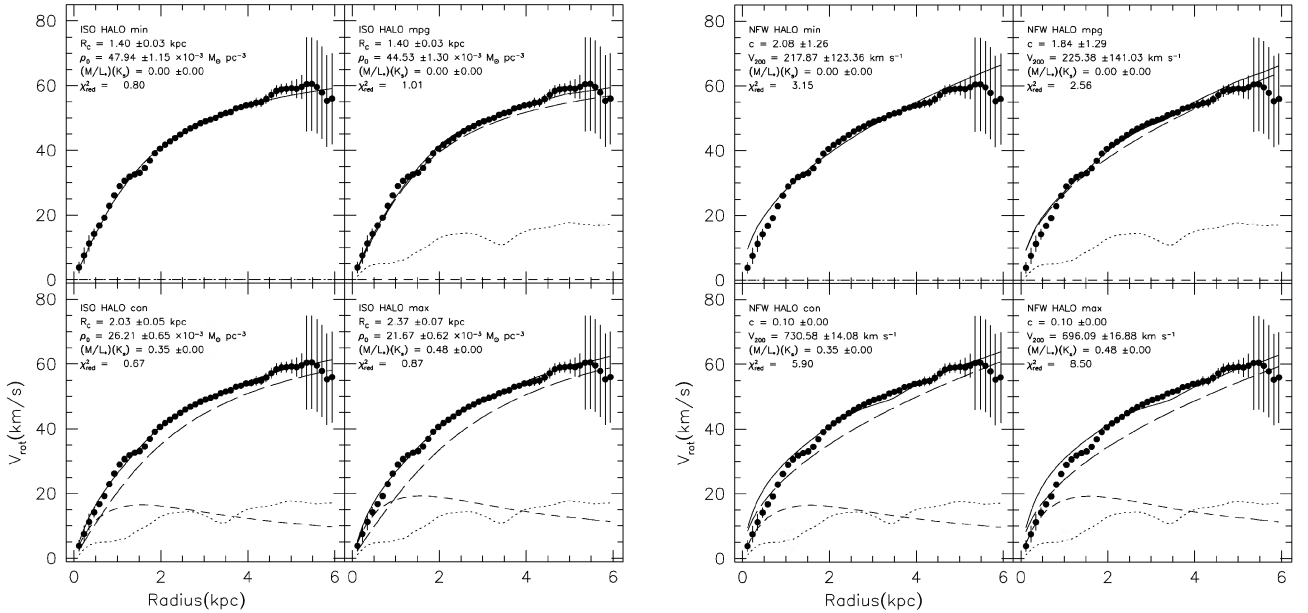


**Figure 13.** B48 mass models. See Fig. 12.

There is a general trend for the value of the maximum disc  $\Upsilon_*$  to decrease with increasing resolution. It is not clear what the cause of this effect is. The inner slopes of the rotation curve and stellar curve change subtly with resolution, but not enough to be the sole cause. It is likely that small differences between the tilted ring models also play a role.

We note that at all resolutions we find that (restricting ourselves to the ISO model for a moment) the min+gas model usually has the smallest value of  $\chi^2$ , and that for all cases  $\chi^2_{\text{min+g}} < \chi^2_{\text{con}}$ . We have

tried to constrain the value of  $\Upsilon_*$  by making a ‘best fit’ to the rotation curves using ISO models: i.e. we also let  $\Upsilon_*$  be a free parameter in the fits. Unfortunately the different resolutions make it difficult to constrain  $\Upsilon_*$  in this manner. The B96 data are best fitted with a stellar component with  $\Upsilon_{*,K} = 0.10 \pm 0.13$ , while the B48 and B24 curves both demand  $\Upsilon_{*,K} = 0.31 \pm 0.04$ . For the B08 and B12 data such a ‘best fit’ gives unphysical results (negative  $\Upsilon_*$ ). A constrained fit with  $\Upsilon_* \geq 0$  yields  $\Upsilon_* = 0$  (i.e. the minimum disc+gas case) as a best fit for these resolutions. Though it is clear that  $\Upsilon_*$  is difficult



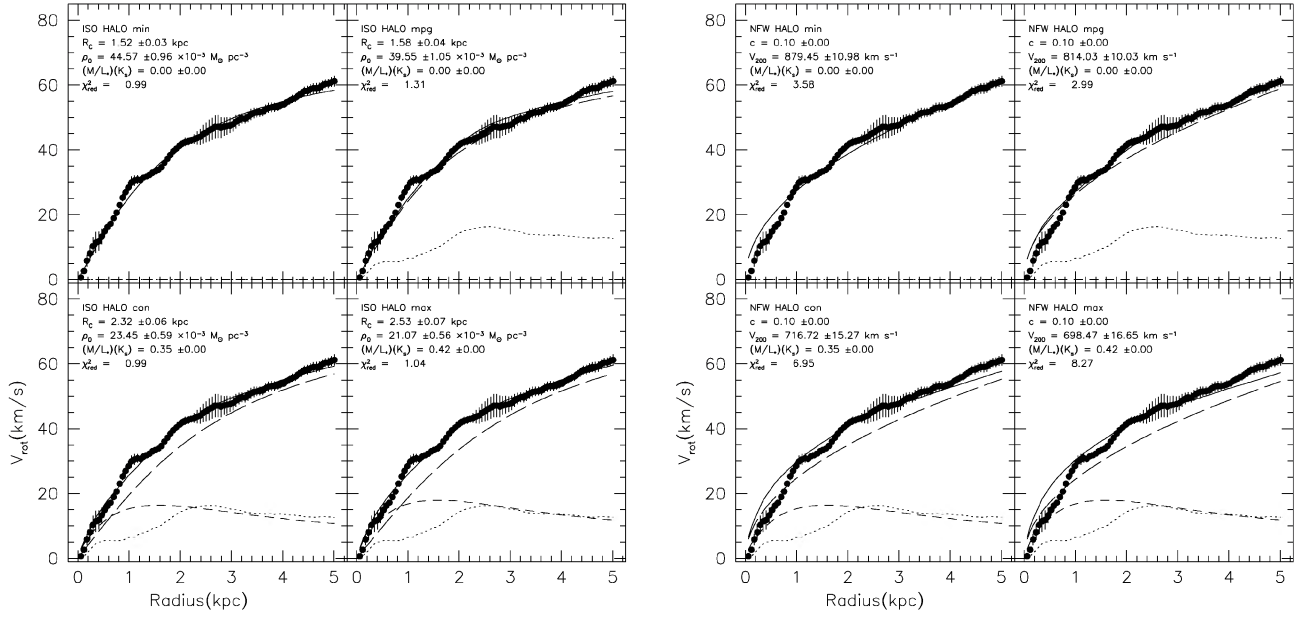


Figure 14. B24 mass models. See Fig. 12.

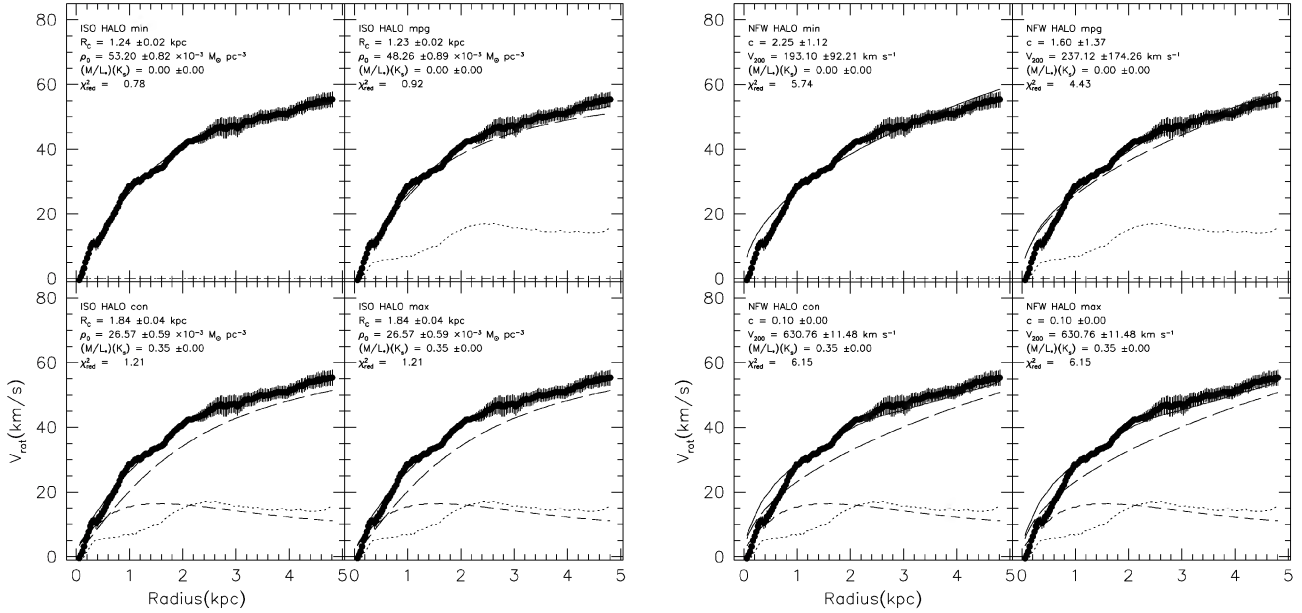


Figure 15. B12 mass models. See Fig. 12.

to constrain using only rotation curve information, the results do suggest that the stellar population is dynamically unimportant.

## 8 DISCUSSION

### 8.1 Inner slopes

With the high-resolution rotation curves we can determine the inner slope of the mass-density distribution. The rationale behind this is described in de Blok et al. (2001b). In summary, the various halo

models make specific predictions concerning the slope of the dark matter mass-density distribution in the inner parts. If we approximate this distribution with a power law  $\rho \sim r^\alpha$ , then the ISO halo predicts  $\alpha = 0$ , while the NFW halo predicts  $\alpha = -1$ . In de Blok et al. (2001b) the inner mass-density slopes of a large sample of LSB galaxies was derived, and the most representative value was  $\alpha = -0.2 \pm 0.2$ , i.e. closer to pseudo-isothermal than to CDM.

Here we derive the slopes of the mass-density distribution of NGC 6822 at various resolutions using the inversion method described in de Blok et al. (2001b) where we compute the mass-density profile and fit a power law to the mass-density profile. Fig. 18 shows two

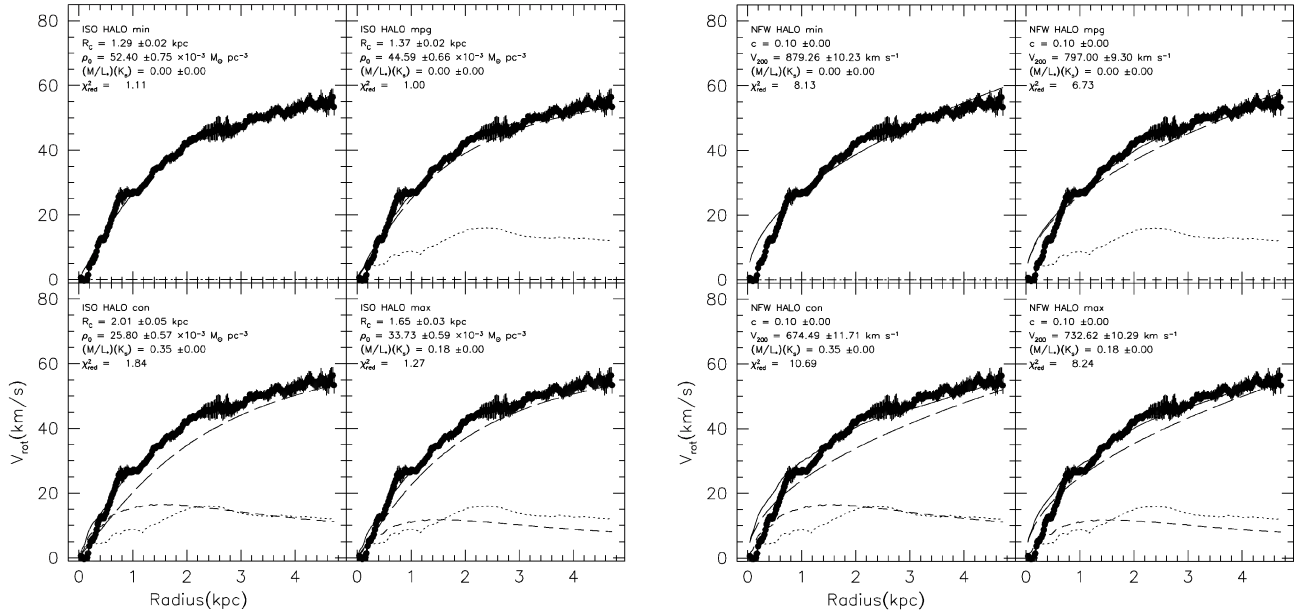


Figure 16. B08 mass models. See Fig. 12.

examples. We show the B96 and B24 mass–density profiles, with the best-fitting NFW and ISO (minimum disc) models overplotted. The NFW models have central densities that are discrepant by a factor of 10 or more.

We measure the slope within  $R = 0.8$  kpc. This is an arbitrary choice, motivated by the fact that we want to use at least three data points to determine the slope of the B96 curve. Other choices are obviously possible, and may result in slightly different values of the slope, but will not affect the conclusions. The resulting values are given in Table 5. For the B08 data a meaningful slope could not be derived because of the large gradients in the rotation velocity that are found at small scales. The values are at significantly different from the NFW values all resolutions. Note that there is no systematic steepening of the slope with resolution, which one would expect if the cusp were hidden by resolution effects. With a resolution of only tens of parsecs it is not clear that there is still room for a cusp in NGC 6822.

## 8.2 Dark matter, feedback and cosmology

In the previous sections we have made NFW fits to the rotation curves disregarding any of the predictions that CDM makes for  $c$ ,  $V_{200}$  and their relation. We will compare the observed rotation curve with cosmological predictions. If we assume that  $V_{200} \simeq V_{\max} \simeq 55 \text{ km s}^{-1}$ , we find for  $\Lambda$ CDM that  $c \simeq 9.5$  (Navarro et al. 1997). The total mass  $M_{200}$  of this halo is  $M_{200} = 5.2 \times 10^{10} M_{\odot}$ . This predicted halo is overplotted on the observed curve in Fig. 19, and overpredicts the rotation velocity in the inner parts by a significant amount.

To look at the problem from a different perspective, let us assume  $\Upsilon_{*} = 0.35$ . This gives a stellar mass  $M_{*} = 1.3 \times 10^8 M_{\odot}$ . The total (atomic) gas mass is  $1.5 \times 10^8 M_{\odot}$  (H I + He) and the total observed baryonic mass is  $2.8 \times 10^8 M_{\odot}$ . A universal baryon fraction of  $\sim 0.09$  (see, e.g., White & Fabian 1995) implies a total mass  $M_{200} = 3.1 \times 10^9 M_{\odot}$ . For a NFW halo this implies  $V_{200} = 21.5 \text{ km s}^{-1}$  and  $R_{200} = 28 \text{ kpc}$ . These values are not consistent with the observed

curve, and imply (apart from the inability of the model to fit the data) that either the baryon fraction in NGC 6822 differs significantly from the universal value or that large amounts of baryons have been expelled, as we will discuss below in more detail.

Let us work out the *observed* matter fractions in NGC 6822. We use the ISO models, and determine the amount of dark matter within a radius of 5 kpc, the outer edge of the H I disc. This yields a total dark mass out to 5 kpc of  $3.2 \times 10^9 M_{\odot}$ . With an observed baryonic mass of  $2.8 \times 10^8 M_{\odot}$  we find that NGC 6822 is heavily dark-matter-dominated with  $M_{\text{vis}}/M_{\text{dark}}(R < 5 \text{ kpc}) = 0.09$ . This is comparable to values found in LSB galaxies and other dwarf galaxies (de Blok & McGaugh 1997). The corresponding baryon fraction is  $f_b = 0.080$ , close to the universal baryon fraction.

The visible matter in NGC 6822 is thus a minor component of the total galaxy system. This makes it harder to explain the observed core-dominated dark matter distribution as resulting from a NFW halo modified by feedback. The term feedback is often used indiscriminately to indicate star formation and evolutionary processes that affect the mass distribution in a galaxy. In fact, there are two distinct forms of feedback. One of them is commonly observed in galaxies, also in NGC 6822, and usually shows itself as small-scale redistribution of mass in the disc.

The second form of feedback is more catastrophic, mostly theoretical, and was introduced to explain the discrepancy between observed and theoretical dark matter distributions. In essence it invokes large-scale and violent star formation, resulting in massive blow-outs that drag dark matter out as a result of gravitational interactions, thus destroying the primordial CDM cusp. The exact physics of feedback are not understood, and the models usually resorts to an empirical description that is fine-tuned to, for example, fit the Tully–Fisher relation or other observational constraints.

Nevertheless, let us explore the implications of feedback: using the amount of energy produced by supernovae and making some standard assumptions one can work out an expression for the amount of matter expelled by the effects of supernovae (see, e.g., equation A4 in van den Bosch et al. 2000). Feedback then requires the

**Table 3.** NFW rotation curve fits.

Resolution	Model	$c$	$\Delta c$	$V_{200}$	$\Delta V_{200}$	$\Upsilon_*$	$\chi^2_{\text{red}}$
B96	min	3.7	1.2	130.2	41.8	0	2.73
	mpg	2.8	1.4	157.0	76.6	0	2.49
	con	0.1	...	810.3	14.1	0.35	2.89
	max	0.1	...	721.9	20.3	0.95	5.97
B96 inner	min	0.1	...	878.0	61.6	0	3.81
	mpg	0.1	...	1791.7	56.7	0	3.24
	con	0.1	...	636.9	57.8	0.35	3.36
	max	0.1	...	377.5	65.7	0.95	4.36
B48	min	2.1	1.3	217.9	123.4	0	3.15
	mpg	1.8	1.3	225.4	141.0	0	2.56
	con	0.1	...	730.6	14.1	0.35	5.91
	max	0.1	...	696.1	16.9	0.48	8.50
B48 inner	min	0.1	...	899.6	26.4	0	5.99
	mpg	0.1	...	826.8	23.6	0	4.82
	con	0.1	...	633.6	33.0	0.35	9.38
	max	0.1	...	563.2	37.1	0.48	11.84
B24	min	0.1	...	879.5	11.0	0	3.58
	mpg	0.1	...	814.0	10.0	0	2.99
	con	0.1	...	716.7	15.3	0.35	6.95
	max	0.1	...	698.5	16.7	0.42	8.27
B24 inner	min	0.1	...	876.5	27.2	0	7.95
	mpg	0.1	...	795.1	24.7	0	6.56
	con	0.1	...	591.3	29.4	0.35	9.31
	max	0.1	...	551.1	30.5	0.42	10.02
B12	min	2.3	1.1	193.1	92.2	0	5.74
	mpg	1.6	1.4	237.1	174.3	0	4.42
	con	0.1	...	630.8	11.5	0.35	6.15
	max	0.1	...	630.8	11.5	0.35	6.15
B12 inner	min	0.1	...	889.3	19.2	0	10.61
	mpg	0.1	...	792.0	17.4	0	8.69
	con	0.1	...	592.4	20.1	0.35	11.65
	max	0.1	...	592.4	20.1	0.35	11.65
B08	min	0.1	...	879.3	10.2	0	8.13
	mpg	0.1	...	797.0	9.3	0	6.73
	con	0.1	...	674.5	11.7	0	10.69
	max	0.1	...	732.6	10.3	0.18	8.24
B08 inner	min	0.1	...	898.7	20.6	0	15.52
	mpg	0.1	...	792.7	19.0	0	13.28
	con	0.1	...	590.7	22.3	0.35	18.11
	max	0.1	...	688.2	20.6	0.18	15.52

Notes. 'min': minimum disc; 'mpg': minimum disc + gas; 'con': constant  $\Upsilon_*$ ; 'max': maximum disc. Dots (...) indicate that the parameter was fixed during fitting.

baryonic mass to drag along a similar amount of dark matter (modulo some efficiency factor that is unlikely to be much larger than unity).

Assuming CDM haloes, we find for  $V_{200} \simeq 55 \text{ km s}^{-1}$  that  $M_{200} = 5.2 \times 10^{10} M_{\odot}$ . Equation (A4) in van den Bosch et al. (2000) then yields that the expelled baryonic mass is  $3.6 \times 10^9 M_{\odot}$ . Assuming that the efficiency factor is unity (every unit mass of baryons drags along one unit mass of dark matter) we find that the amount of dark matter relocated is approximately equal to the amount of dark matter currently observed within the outermost radius of the observed disc. We are thus dealing with a major structural reorganization of a galaxy.

Even if we assume the maximum possible maximum disc  $\Upsilon_* = 0.95$  we still only find an observed baryonic mass of  $5.4 \times 10^8 M_{\odot}$  (though not physically motivated, this is a hard upper limit on the observed baryonic mass). Assuming an efficiency factor of unity, it seems the NGC 6822 must have expelled over  $\sim 6$  times its currently observed baryonic mass.

**Table 4.** ISO rotation curve fits.

Resolution	Model	$R_C$	$\Delta R_C$	$\rho_0$	$\Delta \rho_0$	$\Upsilon_*$	$\chi^2_{\text{red}}$
B96	min	1.63	0.03	42.4	1.1	0	0.18
	mpg	1.71	0.04	37.1	1.1	0	0.24
	con	2.12	0.06	27.1	0.9	0.35	0.28
	max	3.10	0.22	16.7	1.0	0.95	1.08
B96 inner	min	1.50	0.05	45.0	1.2	0	0.05
	mpg	1.47	0.05	41.3	1.2	0	0.05
	con	2.10	0.17	26.4	1.2	0.35	0.10
	max	$\infty$	...	11.2	0.7	0.95	0.55
B48	min	1.40	0.03	47.9	1.2	0	0.80
	mpg	1.40	0.03	44.5	1.3	0	1.01
	con	2.03	0.05	26.2	0.7	0.35	0.67
	max	2.37	0.07	21.7	0.6	0.48	0.87
B48 inner	min	1.22	0.06	53.5	2.6	0	1.19
	mpg	1.12	0.06	53.3	2.9	0	1.17
	con	1.89	0.21	27.2	2.0	0.35	1.55
	max	2.70	0.55	20.3	1.7	0.48	1.95
B24	min	1.51	0.03	44.6	1.0	0	0.99
	mpg	1.58	0.04	39.5	1.0	0	1.31
	con	2.32	0.06	23.4	0.6	0.35	1.00
	max	2.53	0.07	21.1	0.6	0.42	1.04
B24 inner	min	1.31	0.07	49.8	2.1	0	1.06
	mpg	1.20	0.06	48.7	2.2	0	0.96
	con	2.27	0.34	24.1	1.7	0.35	1.60
	max	2.88	0.65	20.6	1.6	0.42	1.84
B12	min	1.24	0.02	53.2	0.8	0	0.78
	mpg	1.23	0.02	48.3	0.9	0	0.92
	con	1.84	0.04	26.6	0.6	0.35	1.21
	max	1.84	0.04	26.6	0.6	0.35	1.21
B12 inner	min	1.19	0.04	55.0	1.7	0	1.53
	mpg	1.06	0.04	54.4	1.8	0	1.35
	con	1.78	0.15	27.2	1.5	0.35	2.50
	max	1.78	0.15	27.2	1.5	0.35	2.50
B08	min	1.29	0.02	52.4	0.8	0	1.11
	mpg	1.37	0.02	44.6	0.7	0	1.00
	con	2.01	0.05	25.8	0.6	0.35	1.84
	max	1.66	0.03	33.7	0.6	0.18	1.27
B08 inner	min	1.43	0.05	49.0	1.2	0	1.81
	mpg	1.39	0.05	44.3	1.3	0	1.73
	con	3.01	0.40	22.2	1.0	0.35	3.06
	max	1.88	0.11	31.5	1.1	0.18	2.21

Notes. 'min': minimum disc; 'mpg': minimum disc + gas; 'con': constant  $\Upsilon_*$ ; 'max': maximum disc.

There has been some discussion in the past as to whether or not stellar feedback can remove a significant fraction of the mass of a galaxy to the intergalactic medium. Gnedin & Zhao (2002), and MacLow & Ferrara (1998) showed that this process is unable to explain the observed cores, and is also inconsistent with other observational constraints. According to numerical simulation of stellar feedback by MacLow & Ferrara (1998) the potential mass loss is a function of the total galaxy mass; for galaxies with gas masses  $< 10^6 M_{\odot}$  a galaxy can potentially destroy itself ('blow-away' scenario), whereas for gas masses between  $10^6$  and  $10^9 M_{\odot}$  some material may be removed ('blow-out', see their fig. 1). According to these models we do not expect significant mass loss in NGC 6822 ( $M_{\text{gas}} = 1.5 \times 10^8$ ) as a result of violent star formation.

From an observer's perspective, there is relatively little evidence that mass loss does indeed occur in dwarf galaxies. Although strong outflow signatures are observed in some cases in dwarf galaxies there are only a few cases where outflow material may permanently escape the galactic gravitational potential (e.g. Martin 1998).

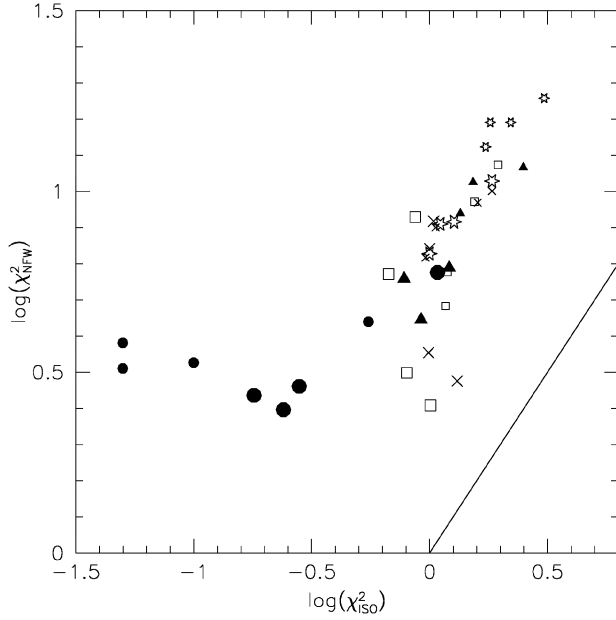


**Figure 17.** Reduced chi2 plot,  $\chi^2(\text{ISO}) < \chi^2(\text{NFW})$  at all resolutions and  $\Upsilon_*$ . The line is the line of equality. Large symbols represent the fits to the complete curves, small symbols fits to the inner curves. Filled circles: B96; open squares: B48; crosses: B24; filled triangles: B12; and stars: B08.

A further problem with expelling a lot of mass is the global dynamics of the galaxy: if one were to have a huge mass loss of the order of a few times the total galaxy mass, one would certainly expect to find some clear evidence in the velocity field. The blown-out gas in such a case is unlikely to end up as an undisturbed regularly rotating H I disc. Furthermore, the stellar record shows no evidence for increases in the star formation rate (SFR) with large factors at any time during the past  $\sim 9$  Gyr (Gallart et al. 1996). It thus seems somewhat surprising that if feedback had occurred, it would have managed to hide all traces of a violent past.

**Table 5.** Inner mass–density slopes.

Resolution	$\alpha$	$\Delta\alpha$
B96	−0.13	0.14
B48	+0.02	0.12
B24	+0.22	0.35
B12	−0.04	0.09
B08	—	—

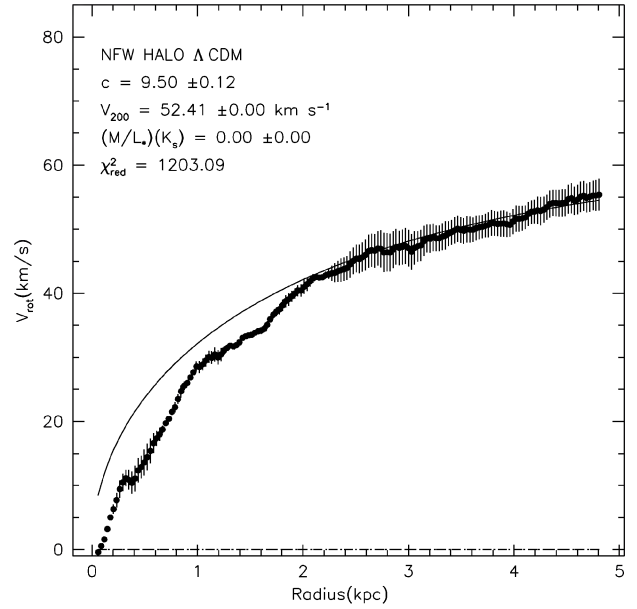


**Figure 19.** Minimum disc halo for B12 using parameters as required by CDM simulations assuming that  $V_{\text{max}} = V_{200}$ .

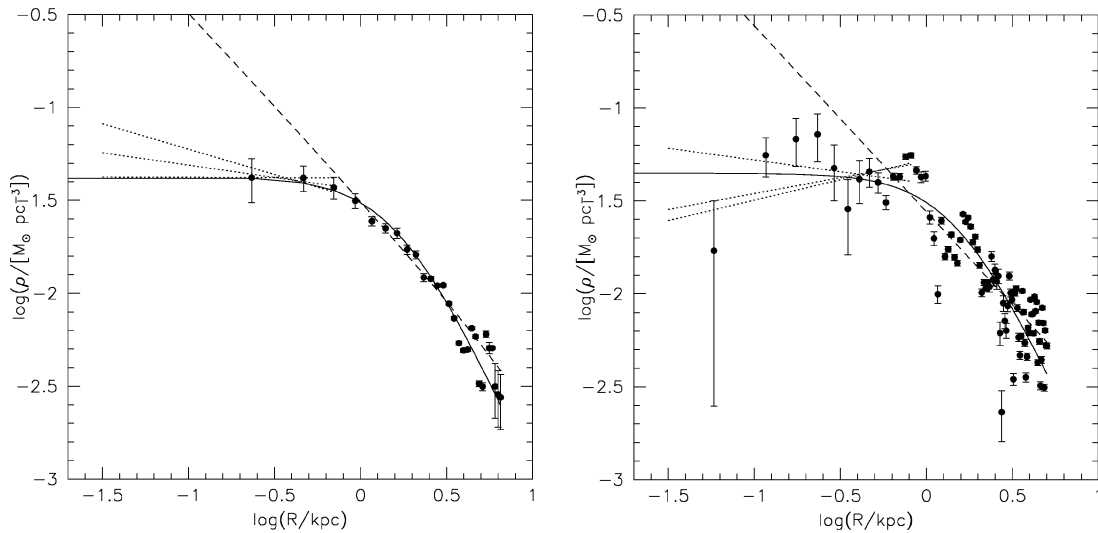


**Figure 18.** Mass–density profiles for the B96 (left) and B24 (right) models. The long-dashed lines shows the best-fitting minimum disc NFW model and the full line shows the best-fitting ISO model. The dotted lines represent the power-law fits to the data at  $R < 0.8$  kpc.



In summary, we conclude that potential feedback of several times the total baryonic mass of NGC 6822 is unlikely. The observed rotation curve of NGC 6822, combined with the *K*-band and H I data thus lead to a picture that is inconsistent with a combination of cuspy halo and feedback.

## 9 CONCLUSIONS

We obtained high-resolution rotation curves for the Local Group dwarf irregular galaxy NGC 6822. By fitting both pseudo-isothermal and NFW halo models, it was found that the pseudo-isothermal model fits the data successfully. NGC 6822 is not maximum disc and is dominated by dark matter. The highest-resolution rotation curve has some 250 independent points and beam-smearing effects are not an issue. The position of the dynamical centre is unambiguously determined. There is no indication of a dark matter cusp down to scales of  $\sim 20$  pc.

Trying to explain the observed curve with a combination of feedback and CDM haloes leads to several inconsistencies. Feedback and CDM seem to imply that NGC 6822 has lost approximately six times the currently observed number of baryons. There is, however, no evidence for such violent processes. We therefore conclude that (i) the dark matter distribution in NGC 6822 is unlikely to have been affected by feedback and (ii) is best described by a model with a constant-density core.

## ACKNOWLEDGMENTS

We thank Steve Schneider for providing us with the 2MASS images. We thank Sébastien Blais-Ouellette for constructive comments that helped to improve this paper. This publication makes use of data products from the Two Micron All-sky Survey, which is a joint project of the University of Massachusetts and the Infrared Processing and Analysis Centre/California Institute of Technology, funded by the National Aeronautics and Space Administration and the National Science Foundation.

## REFERENCES

- Begeman K., 1987, PhD thesis, Univ. of Groningen  
 Bell E.F., de Jong R.S., 2000, MNRAS, 312, 497  
 Blais-Ouellette S., Amram P., Carignan C., 2001, AJ, 121, 1952  
 Bolatto A.D., Simon J.D., Leroy A., Blitz L., 2002, ApJ, 565, 238  
 Bottima R., 1997, A&A, 328, 517  
 Casertano S., 1983, MNRAS, 203, 735  
 de Blok W.J.G., Bosma A., 2002, A&A, 385, 816  
 de Blok W.J.G., McGaugh S.S., 1997, MNRAS, 290, 533  
 de Blok W.J.G., Walter F., 2000, in Kraan-Korteweg R.C., Henning P.A., Andernach H., eds, ASP Conf. Proc. Vol. 218, Mapping the Hidden Universe: the Universe Behind the Milky Way – the Universe in HI. Astron. Soc. Pac., San Francisco, p. 357  
 de Blok W.J.G., Walter F., 2001, ApJ, 537, L95  
 de Blok W.J.G., van der Hulst J.M., Bothun G.D., 1995, MNRAS, 274, 235  
 de Blok W.J.G., McGaugh S.S., Rubin V., 2001a, AJ, 122, 2396  
 de Blok W.J.G., McGaugh S.S., Bosma A., Rubin V., 2001b, ApJ, 552, L23  
 de Jong R.S., 1996, A&A, 313, 377  
 Dubinski J., Carlberg R.G., 1991, ApJ, 378, 496  
 Gallart C., Aparicio A., Bertelli G., Chiosi C., 1996, AJ, 112, 2596  
 Gerritsen J.P.E., de Blok W.J.G., 1999, A&A, 342, 655  
 Gnedin O.Y., Zhao H.-S., 2002, MNRAS, 333, 299  
 Grebel E.K., 2001, ApSSS, 277, 231  
 Hodge P.W., 1980, ApJ, 241, 125  
 Hodge P., Smith T., Eskridge P., MacGillivray H., Beard S., 1991, ApJ, 379, 621  
 Israel F.P., Bontekoe Tj. R., Kester D.J.M., 1996, A&A, 308, 723  
 Lake G., Feinswog L., 1989, AJ, 98, 166  
 MacLow M.-M., Ferrara A., 1998, ApJ, 513, 142  
 McGaugh S.S., Rubin V., de Blok W.J.G., 2001, AJ, 122, 2396  
 Martin C.L., 1998, ApJ, 506, 222  
 Mateo M.L., 1998, ARA&A, 36, 435  
 Moore B., 1994, Nat, 370, 629  
 Navarro J.F., Frenk C.S., White S.D.M., 1996, ApJ, 462, 563  
 Navarro J.F., Frenk C.S., White S.D.M., 1997, ApJ, 490, 493  
 Skillman E.D., Terlevich R., Melnick J., 1989, MNRAS, 240, 563  
 Swaters R.A., 1999, PhD thesis, Univ. of Groningen  
 Swaters R.A., Madore B.F., Trewheella M., 2000, ApJ, 531, L107  
 van Albada T. S., Sancisi R., 1986, Phil. Trans. R. Soc. Lond. A, 320, 447  
 van den Bosch F.C., Robertson B.E., Dalcanton J.J., de Blok W.J.G., 2000, AJ, 119, 1579  
 van der Kruit P.C., Searle L., 1981, A&A, 95, 105  
 Verheijen M.A.W., 1997, PhD thesis, Univ. of Groningen  
 White D.A., Fabian A.C., 1995, MNRAS, 273, 72

This paper has been typeset from a  $\text{\LaTeX}$  file prepared by the author.